Check for updates

Constructing highly durable reversal-tolerant anodes *via* integrating high-surface-area Ti_4O_7 supported Pt and Ir@IrO$_x$ for proton exchange membrane fuel cells†

Zheng Li, [ID] [abc] Yongbiao Mu, [bc] Qing Zhang, [bc] Haodong Huang, [bc] Xianbin Wei, [d] Lin Yang, [bc] Guanxiong Wang, [e] Tianshou Zhao, [ID] *[abc] Gang Wu [ID] *[f] and Lin Zeng [ID] *[bc]

Fuel starvation during the fuel cell operation inevitably leads to high potential anodes, which causes carbon corrosion and catalyst layer collapse and poses a challenge to the durability of proton exchange membrane fuel cells. Herein, Ti_4O_7 with a high specific surface area was synthesized facilely and utilized to replace carbon as the anode catalyst support. Previously, the initial performance of the Ti_4O_7-supported catalyst was obstructed by the disadvantaged electrical conductivity of Ti_4O_7. This work obtains a comparable polarization performance after optimizing the Ti_4O_7-supported anode catalyst layer parameters by shortening the electron transfer pathway and increasing metal coverage. Meanwhile, reversal-tolerant anodes (RTAs) were fabricated by the traditional IrO_2 addition and core–shell structured Ir@IrO$_x$ to validate the applicability of the Ti_4O_7 support. Typically, the Ir@IrO$_x$/Pt/Ti_4O_7-fabricated RTA with low Ir loading displays an approximately ten times longer reversal time (6 hours) and two orders of magnitude lower degradation rate than a conventional carbon-supported counterpart. The degradation origin of the Ti_4O_7-supported anodes was also studied by postmortem characterizations, pointing to the Pt oxidation caused by the formation of TiO_x thin layers on the Pt surface. The study aims to promote the development of carbon-free anodes and provide a bright perspective for practical high-performance, low-degradation, and cost-friendly RTA fabrication.

Broader context

Durability and cost are essential factors for the commercial application of proton exchange membrane fuel cells (PEMFCs). Anode cell reversal happens inevitably during the operation of PEMFCs and causes irreversible damage to the anode catalyst layer. Commercially, IrO_2 or Ir black is utilized to alleviate the destruction of cell reversal even though it deteriorates the performance and increases the cost. Hence, an enhanced anode is highly desired for practical PEMFCs to address commercial issues. This work is dedicated to the development of a high-performance, low-degradation, and cost-friendly anode through integrating high-surface-area Ti_4O_7 supported Pt and core–shell structured Ir@IrO$_x$ to significantly improve the reversal tolerance while maintaining polarization performance with super-low degradation. Through postmortem studies, along with advanced characterization, the degradation mechanisms of carbon-supported and Ti_4O_7-supported catalysts are comprehensively compared. This work represents the most promising carbon-free support candidate and paves the way for future research of reversal tolerance anodes for PEMFCs.

[a] Department of Mechanical and Aerospace Engineering, The Hong Kong University of Science and Technology, Clear Water Bay, Kowloon, Hong Kong, China. E-mail: zhaots@sustech.edu.cn

[b] Shenzhen Key Laboratory of Advanced Energy Storage, Department of Mechanical and Energy Engineering, Southern University of Science and Technology, Shenzhen 518055, China. E-mail: zengl3@sustech.edu.cn
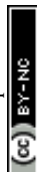
[c] SUSTech Energy Institute for Carbon Neutrality, Southern University of Science and Technology, Shenzhen 518055, China

[d] Department of Materials Science and Engineering, Southern University of Science and Technology, Shenzhen 518055, Guangdong, China

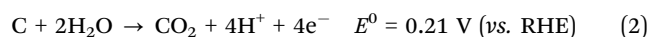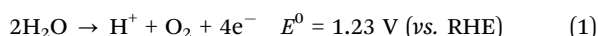*[e] Shenzhen Academy of Aerospace Technology, Shenzhen 518057, China*

[f] Department of Chemical and Biological Engineering, University at Buffalo, The State University of New York, Buffalo, New York 14260, USA. E-mail: gangwu@buffalo.edu

† Electronic supplementary information (ESI) available. See DOI: https://doi.org/10.1039/d3ee03921h

1580 | *Energy Environ. Sci.*, 2024, **17**, 1580–1591

This journal is © The Royal Society of Chemistry 2024

1. Introduction

Driven by the growing demand for carbon-free energy, the "hydrogen society" concept has been put forward toward the "carbon neutral" goal. Among all hydrogen energy utilization units, proton exchange membrane fuel cells (PEMFCs) are the most promising for commercialization, attracting intensive attention and investigation.[1] However, durability and cost are the main hindrances to broader commercialization.[2] Among all the problems, the cell reversal would damage the anode catalyst layer and further reduce durability. In particular, due to the local fuel starvation, the potential between the anode and cathode is narrowing or even reversing during the cell reversal. The carbon oxidation reaction (COR) and oxygen evolution reaction (OER) happen to maintain the external current and internal proton flow instead of the initially desirable hydrogen oxidation reaction (HOR), while the oxygen reduction reaction (ORR) remains unchanged in the cathode.[3] Notably, the COR is more harmful than the OER because the irreversible corrosion of carbon leads to the detachment of Pt nanoparticles,[4] increased internal resistance,[5] and the collapse of the catalyst layer,[6] significantly deteriorating performance.[7]

$$2H_2O \rightarrow H^+ + O_2 + 4e^- \quad E^0 = 1.23 \text{ V } (vs. \text{ RHE}) \quad (1)$$

$$C + 2H_2O \rightarrow CO_2 + 4H^+ + 4e^- \quad E^0 = 0.21 \text{ V } (vs. \text{ RHE}) \quad (2)$$

$$C + H_2O \rightarrow CO + 2H^+ + 4e^- \quad E^0 = 0.52 \text{ V } (vs. \text{ RHE}) \quad (3)$$

Fuel cell system control strategies are applied to prevent fuel starvation. However, the system control is always hysteretic due to the distributed effect of the large effective area of commercial single cells and the porous structure of the electrode. It is still necessary to improve the corrosion resistance of electrodes. Applying a more stable material as the catalyst support is a practical strategy to eliminate the performance loss caused by carbon corrosion.[8] Among all potential candidates, titanium suboxides (also known as the Magneli phase, Ti_nO_{2n-1}), especially Ti_4O_7, attract great attention since it owns a wider electrochemical stability window,[9] relatively high electrical conductivity,[10] and excellent stability under fuel cell operating environments.[11] Traditionally, Ti_4O_7 is synthesized by reducing TiO_2 under pure or dilute hydrogen at a high temperature, which is dangerous in laboratory or commercial scale-up production since hydrogen is a flammable and explosive gas with a wide explosive limit. The obtained Ti_4O_7 typically displays a low specific surface area (less than 10 m² g⁻¹) with micro-scale size.[12,13] The dangerous synthesis and the sintering aggregation properties hinder the application of Ti_4O_7 as the fuel cell catalyst support. In addition, the initial performance loss is inevitable for titanium oxide-supported catalysts due to the disadvantage of electronic conductivity compared to carbon.[14] Previous research tends to apply super-high anode Pt loadings to cover up the initial performance loss, such as 0.4 mg_{Pt} cm⁻² [15] and 0.5 mg_{Pt} cm⁻²,[16] which is far from the practical application. Alternatively, carbon is added into titanium oxide-supported catalyst layers to offset the unsatisfactory electronic conductivity.[17–20] However, carbon corrosion during the cell

reversal is inevitable once the carbon exists and thus causes performance decay.

In this work, we synthesized a pure Ti_4O_7 anode with a high specific surface area by a facile hydrogen-free method. After the Pt deposition, the Pt/Ti_4O_7 anode at a 0.1 mg_{Pt} cm⁻² loading exhibited comparable performance to a commercial Pt/C catalyst under different operating conditions. The key to improving Ti_4O_7-supported catalyst layer performance is shortening the electronic transfer pathway and increasing the metal coverage on the Ti_4O_7 surface, achieved by constructing a thin catalyst layer and high Pt content in the anode. Traditional IrO_2 addition and novel $Ir@IrO_x$ core–shell Ir deposition were applied to fabricate reversal-tolerant anodes (RTAs) to boost OER activity. The results showed that the membrane electrode assembly (MEA) with the Ti_4O_7-supported catalyst effectively prolonged the first reversal time and decreased the performance degradation rate. The performance degradation was investigated, and the results indicate that the degradation originates from the Pt oxidation by forming a TiO_x thin layer at the Pt surface, verified by postmortem EIS, XPS, SEM, and TEM characterization.

2. Results and discussion

2.1 Ti_4O_7 synthesis and optimization of catalyst layer parameters

The procedure applied to synthesize Ti_4O_7 is illustrated in Fig. 1a. The XRD patterns under different synthesis conditions are presented in Figure S1 to confirm the synthesis of Ti_4O_7. When the mass ratio of PEG 400 to $TiOSO_4$ (based on TiO_2) is 1, the diffraction peaks of the (110) and (211) facets of TiO_2 appear at 27.4° and 54.3°, indicating over-oxidation during synthesis. The mass ratio of PEG400 to $TiOSO_4$ (based on TiO_2) was increased to 1.5 for a thicker PEG 400 coating, resulting in significantly attenuated TiO_2 peak intensities. Furthermore, particles near the gas flow aggregated together and turned white due to uneven gas flow distribution and exposure to high temperatures. Therefore, the PEG@TiO_2 powder was ground with an agate mortar and then placed in a sealed quartz crucible before heating. The XRD analysis revealed that the grinding and sealing processes effectively inhibit TiO_2 formation and promote the desirable Ti_4O_7 phase. Due to the difference in properties between Ti_4O_7 and carbon, the Pt/Ti_4O_7 anode catalyst layer parameters were optimized, including Pt content, ionomer content, and Pt loading. First, the Pt content of Pt/Ti_4O_7 was controlled by the mass ratio of Pt precursor to Ti_4O_7 in the synthesis process. A higher Pt coverage on the Ti_4O_7 surface can reduce the Ti_4O_7 exposure and form a connected metal nanoparticle network, creating a potential electron transfer pathway and offsetting the disadvantaged conductivity. Based on the observations made during the synthesis process, the product yield is higher (over 90%) when the Pt content is 20% to 40%. However, if the Pt content is increased to 50%, the product yield drops significantly to 81.3%. This indicates a considerable mass loss for
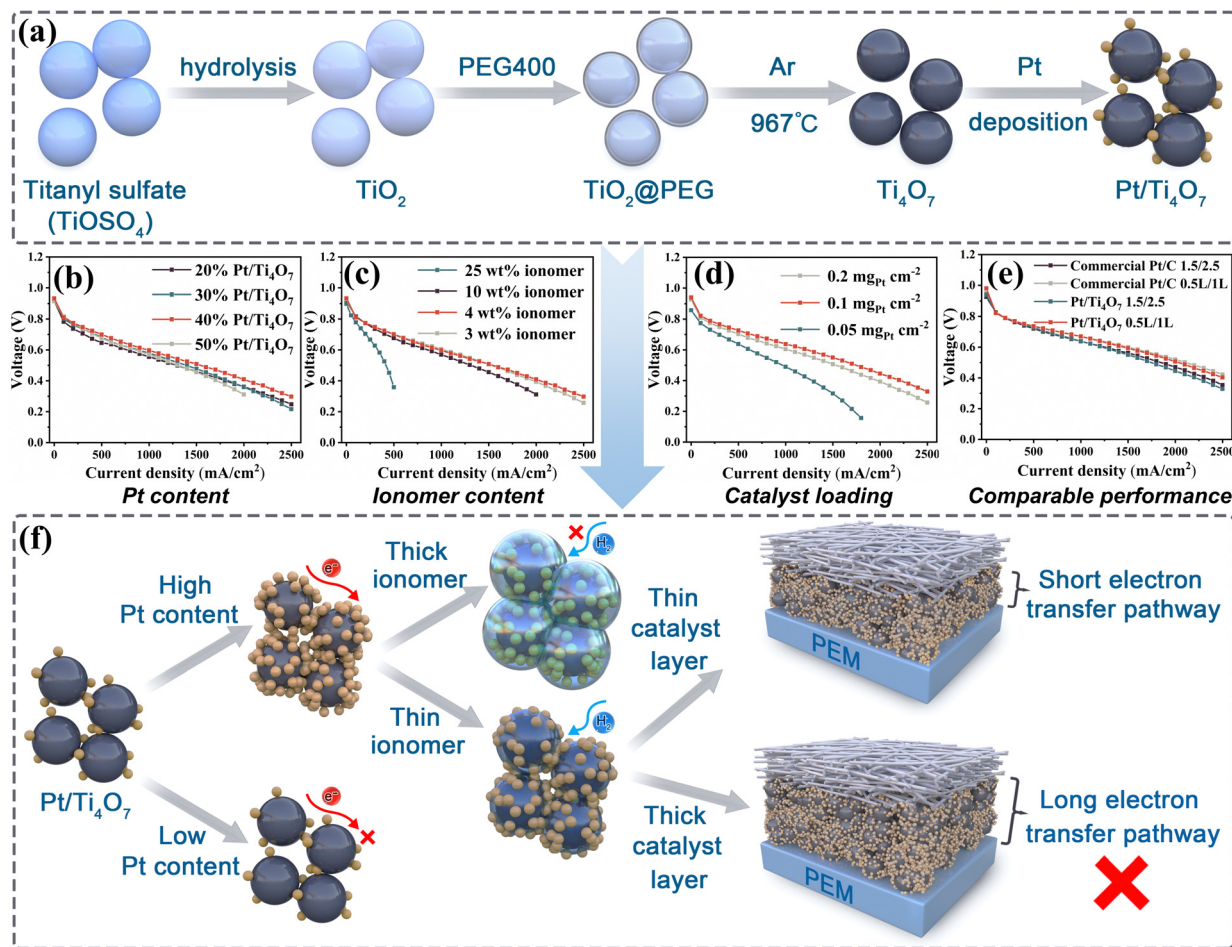
This journal is © The Royal Society of Chemistry 2024

Energy Environ. Sci., 2024, **17**, 1580–1591 | 1581

Fig. 1 (a) Schematic diagram of the synthesis procedure of Pt/Ti$_4$O$_7$. H$_2$/air polarization curves of Pt/Ti$_4$O$_7$ anodes under different (b) Pt contents, (c) ionomer contents, and (d) Pt loadings. (e) Comparison of commercial Pt/C and Pt/Ti$_4$O$_7$ under stoichiometry flows (1.5/2.5) and fixed flows (0.5 L/1 L). (f) Summary of the Pt/Ti$_4$O$_7$ anode catalyst layer parameter optimization principle.

50% Pt/Ti$_4$O$_7$ during the synthesis. Therefore, the complete surface loading of Ti$_4$O$_7$ is 40% Pt/Ti$_4$O$_7$, while for 50% Pt/Ti$_4$O$_7$, there is an over-Pt loading. The overloading of Pt causes the aggregation of Pt and decreases the Pt utilization, making it difficult for Pt deposition. The polarization curves of 20% to 50% Pt/Ti$_4$O$_7$ anodes are shown in Fig. 1b, further confirming the optimization of Pt content at 40%. The performance of Pt/Ti$_4$O$_7$ is also significantly impacted by the ionomer content. As demonstrated in Fig. 1c, the polarization performance improves noticeably when the ionomer content decreases from 25 wt% to 4 wt% due to the thinner ionomer layer. However, when the ionomer content decreases to 3 wt%, the performance declines, particularly in the large current density range. This can be attributed to the limited proton transfer ability caused by the low ionomer content at this stage. Subsequently, the Pt loading was investigated and optimized. As shown in Fig. 1d, the Pt/Ti$_4$O$_7$ anode with 0.1 mg$_{Pt}$ cm^{-2} displays the highest polarization performance compared to 0.2 mg$_{Pt}$ cm^{-2} and 0.05 mg$_{Pt}$ cm^{-2}. A similar outcome was observed in other titanium oxide-supported catalysts.[15] The MEA with a Pt/C anode with different Pt loadings was also tested. As shown in

Fig. S2 (ESI†), Pt/C anodes with 0.1 and 0.2 mg$_{Pt}$ cm^{-2} exhibit similar polarization performance, indicating an anode loading of 0.1 mg$_{Pt}$ cm^{-2} is sufficient, and the cathode limits the performance. However, when the Pt loading further decreases to 0.05 mg$_{Pt}$ cm^{-2}, the performance decay with more than 100 mV loss at 1000 mA cm^{-2} is observed due to the limited active site of the anode, implying 0.1 mg$_{Pt}$ cm^{-2} is also the optimized loading of Pt/C in the anode catalyst layer. Eventually, the optimized parameters of the Pt/Ti$_4$O$_7$ anode catalyst layer are determined as a Pt content of 40 wt%, an ionomer content of 4 wt%, and a Pt loading of 0.1 mg$_{Pt}$ cm^{-2}. Under these conditions, the Pt/Ti$_4$O$_7$ anode catalyst layer showed similar polarization performance to commercial Pt/C under different flow rates. Specifically, at 1000 mA cm^{-2} under 0.5 L/1 L fixed flows, the Pt/Ti$_4$O$_7$ anode catalyst layer achieved a polarization voltage of 0.670 V compared to 0.673 V for the commercial Pt/C. Similarly, at 1000 mA cm^{-2} under 1.5/2.5 stoichiometry flows, the Pt/Ti$_4$O$_7$ anode catalyst layer achieved a polarization of 0.638 V compared to 0.639 V for the commercial Pt/C (Fig. 1e). The high specific surface area of Ti$_4$O$_7$ enables a high Pt content Pt/Ti$_4$O$_7$ anode and further results in a thinner catalyst layer at a given Pt

1582 | *Energy Environ. Sci.*, 2024, **17**, 1580–1591

This journal is © The Royal Society of Chemistry 2024

Fig. 2 (a) Schematic diagram of the synthesis procedure of Ir@IrO$_x$/Pt/Ti$_4$O$_7$. (b, c) TEM images of Ti$_4$O$_7$ and the corresponding EDS mapping. (d) N$_2$ adsorption and desorption isotherms of XC-72R and Ti$_4$O$_7$. (e) and (f) HR-TEM images of 40% Pt/Ti$_4$O$_7$. (g) XRD patterns of carbon-supported and Ti$_4$O$_7$-supported catalysts. (h) and (i) TEM images of Ir@IrO$_x$/Pt/Ti$_4$O$_7$ and (j) the corresponding EDS mapping. (k) XPS Pt 4f and Ir 4f spectra of Ir@IrO$_x$/Pt/Ti$_4$O$_7$. (l) XPS depth profiles of Ir 4f for Ir@IrO$_x$/Pt/Ti$_4$O$_7$ with various Ar sputtering times.

while the Ir(ɪᴠ) 4f peaks present at 61.7 eV and 64.7 eV, and the Ir(ɪɪɪ) 4f peaks appear at 62.6 eV and 65.6 eV.[24] According to the deconvolution analysis of Pt 4f and Ir 4f spectral peaks, Pt(0) and Ir(ɪᴠ) present a dominant percentage even though Pt(ɪɪ), Pt(ɪᴠ), Ir(0), and Ir(ɪɪɪ) also exist. A similar test was conducted for Ir@IrO$_x$/Pt/C to eliminate the Ir–O interaction between Ti$_4$O$_7$ and Ir. As shown in Fig. S10 (ESI†), the Ir(ɪᴠ) is still dominant compared with Ir(ɪɪ) and Ir(0), suggesting the existence of IrO$_x$ species. To further confirm the structure of the Ir species, XPS tests were performed at various sputtering depths to reveal the Ir valence state distribution, and the results are shown in Fig. 2l. The sputtering depth interval is 0.025 nm for each

adjacent XPS Ir 4f spectrum, and the total sputtering depth is 0.25 nm. The Ir 4f$_{7/2}$ and 4f$_{5/2}$ peaks show negative core-level shifts during continuous etching when the sputtering depth is below 0.1 nm, displaying a higher Ir(0) 4f peak area ratio. The reason can be explained by the surface oxidation of Ir nanoparticles and the oxidation layer thickness is approximately 0.1 nm. When the sputtering depth keeps on increasing up to 0.25 nm, the Ir 4f peaks remain almost unchanged, implying the metallic Ir dominates inside, which is consistent with the XRD results. Considering the metallic Ir XRD diffraction peaks, metallic Ir lattice space observed in TEM images and surface Ar sputtering of XPS analysis, it can be concluded that the external

1584 | *Energy Environ. Sci.*, 2024, **17**, 1580–1591

This journal is © The Royal Society of Chemistry 2024

Ir on the particle surface is oxidized, while the inner Ir remains in the metallic state, indicating the core–shell Ir@IrO$_x$ structure.

2.3 Electrochemical results of Ti$_4$O$_7$-supported catalysts

The electrochemical performance was evaluated by the half-cell tests and MEA full-cell tests. First, linear sweep voltammetry (LSV) was conducted to assess the HOR and OER activities. As shown in Fig. 3a, Pt/Ti$_4$O$_7$ exhibits satisfactory HOR activity similar to the commercial Pt/C, with diffusion-limited plateaus reached within 70 mV. Meanwhile, IrO$_2$ can hardly oxidize hydrogen below 0.3 V (vs. RHE), indicating little contribution to the anode HOR activity. As presented in Fig. 3b, the OER activity test demonstrated that Ir@IrO$_x$/Pt/C and Ir@IrO$_x$/Pt/Ti$_4$O$_7$ share almost identical activity. Commercial IrO$_2$ displayed a larger overpotential than Ir@IrO$_x$/Pt/C and Ir@IrO$_x$/Pt/Ti$_4$O$_7$ (390 mV vs. 360 mV@10 mA cm^{-2}) due to the larger

particle size and lower catalyst utilization. The OER activity of Pt/C is also sluggish below 1.7 V (vs. RHE), implying the majority of OER activity of the RTA comes from the Ir. For better comparison with Ti$_4$O$_7$ and carbon supports, the polarization performance tests at the stoichiometry flow (1.5/2.5) before and after the reversal tests were performed by traditionally adding commercial IrO$_2$ to form Pt/C + IrO$_2$ and Pt/Ti$_4$O$_7$ + IrO$_2$ reversal tolerance anodes, as shown in Fig. 3d. Similarly, the polarization performances of Ir@IrO$_x$/Ti$_4$O$_7$ and Ir@IrO$_x$/Pt/C fabricated RTAs are presented in Fig. 3e. In addition, the reversal tests were performed, and the results are displayed in Fig. 3c. Initially, no significant performance difference is observed for Pt/C + IrO$_2$ and Pt/Ti$_4$O$_7$ + IrO$_2$ RTAs before the reversal tests with the maximum power density of 915 and 937 mW cm^{-2} (0.606 V vs. 0.613 V @ 1000 mA cm^{-2}). The reversal tests were also conducted, and the Pt/Ti$_4$O$_7$ + IrO$_2$ RTA can achieve a reversal time four times longer than
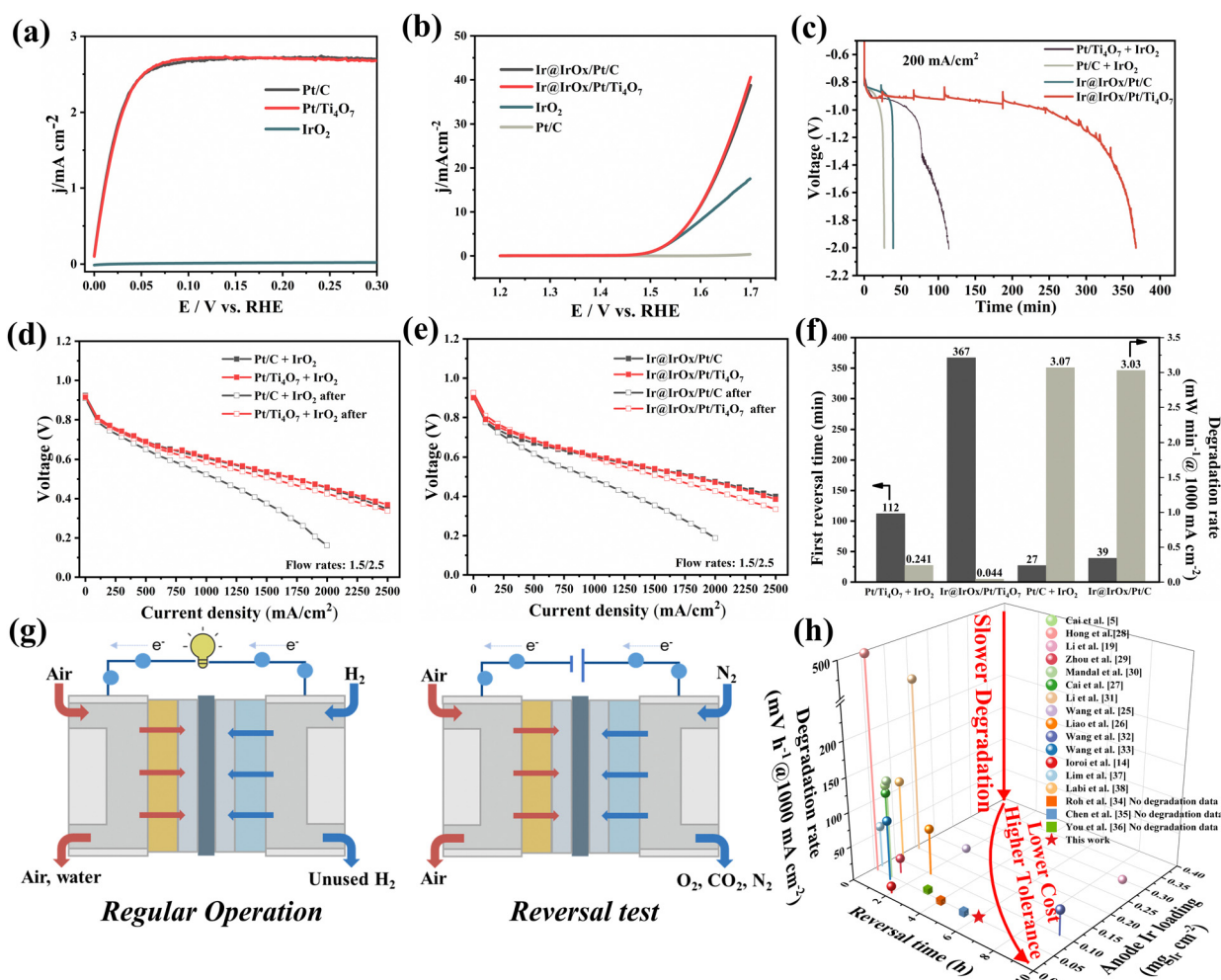
Fig. 3 (a) HOR polarization curves of Pt/Ti$_4$O$_7$, the commercial Pt/C, and the commercial IrO$_2$ in H$_2$-saturated 0.1 M HClO$_4$, (b) OER polarization curves of Ir@IrO$_x$/Pt/C, Ir@IrO$_x$/Pt/Ti$_4$O$_7$, commercial Pt/C and commercial IrO$_2$ in N$_2$-saturated 0.5 M H$_2$SO$_4$ at a scan rate of 5 mV s^{-1} and rotational speed of 1600 rpm. (c) Reversal tolerance test and H$_2$/air polarization curves of (d) Pt/C + IrO$_2$ and Pt/Ti$_4$O$_7$ + IrO$_2$, (e) Ir@IrO$_x$/Pt/C and Ir@IrO$_x$/Pt/Ti$_4$O$_7$ RTAs under stoichiometry flows (1.5/2.5). (f) Comparison of reversal times and maximum power density degradation rates under fixed flows. (g) Schematic illustration of the anode reversal test. Components from left to right: cathode flow field plate, CGDL, CCL, PEM, ACL, AGDL, and anode flow field plate. (h) The comparison of anode Ir loading, first reversal time and degradation rate with recently reported literature.

the Pt/C + IrO$_2$ RTA (112 min $vs.$ 27 min). The period between 1.4 V and 2.0 V is prominently longer for the Pt/Ti$_4$O$_7$ + IrO$_2$ RTA due to the enhanced anti-corrosion ability of Ti$_4$O$_7$. The polarization performance after the reversal test is also shown in Fig. 3d, and the results show that the Pt/C + IrO$_2$ RTA loses approximately 38% performance in 27 min (from 915 to 573 mW cm^{-2} and from 0.606 V to 0.523 V @ 1000 mA cm^{-2}). Meanwhile, the Pt/Ti$_4$O$_7$ + IrO$_2$ RTA displays about 92% performance retention after a 112 min reversal time (from 937 to 860 mW cm^{-2} and from 0.613 V to 0.586 V @ 1000 mA cm^{-2}), suggesting that using Ti$_4$O$_7$ as the catalyst support can effectively prolong the reversal time and protect the catalyst layer structure. Likewise, in terms of the Ir@IrO$_x$/Pt/C and Ir@IrO$_x$/Ti$_4$O$_7$ RTAs, similar initial performances are presented with a maximum power density of 1000 and 973 mW cm^{-2} (0.603 V $vs.$ 0.609 V @ 1000 mA cm^{-2}). For the Ir@IrO$_x$/Pt/C RTA, the voltage reaches the terminal voltage in 39 min, while that of the Ir@IrO$_x$/Pt/Ti$_4$O$_7$ RTA does not drop rapidly but is maintained up to 367 min, which is nearly ten times longer than that of the Ir@IrO$_x$/Pt/C RTA. The postmortem performances were also tested to evaluate the degradation of Ir@IrO$_x$/Pt/Ti$_4$O$_7$ and Ir@IrO$_x$/Pt/C RTAs. Regarding the Ir@IrO$_x$/Pt/C RTA, noticeable performance loss was observed even though the reversal time is significantly shorter than that of the Ir@IrO$_x$/Pt/Ti$_4$O$_7$ RTA, as shown in Fig. 3e. The maximum power density of Ir@IrO$_x$/Pt/C decreases apparently by 467 mW cm^{-2}, from 1000 mW cm^{-2} to 533 mW cm^{-2} (from 0.603 V to 0.485 V @ 1000 mA cm^{-2}), showing a 47% performance loss in half-hour of cell reversal duration. By contrast, the Ir@IrO$_x$/Pt/Ti$_4$O$_7$ RTA presents a better performance retention ability, and the maximum power density reduces by 112 mW cm^{-2}, from 973 mW cm^{-2} to 861 mW cm^{-2} (from 0.609 V to 0.593 V @ 1000 mA cm^{-2}), with 88% performance retention after more than six hours of cell reversal test. The situation is similar when applying the fixed flow (0.5/1 L min^{-1}), as shown in Fig. S11 (ESI†). Sufficient flows are provided to minimize the effect of catalyst layer thickness since Ti$_4$O$_7$ has a much larger mass weight when compared with carbon, which means a thinner catalyst layer thickness. Based on the similar initial performance, the Ir@IrO$_x$/Pt/Ti$_4$O$_7$ and Pt/Ti$_4$O$_7$ + IrO$_2$ RTAs can maintain 85% and 90% maximum power density after the reversal test. The first reversal times and degradation rates of the four anode MEAs are summarized in Fig. 3f. The Ti$_4$O$_7$-supported RTAs display a significantly longer reversal time and two orders of magnitude lower degradation rates than carbon-supported counterparts. Particularly, Ir@IrO$_x$/Pt/Ti$_4$O$_7$ and Pt/Ti$_4$O$_7$ + IrO$_2$ RTAs present 0.044 and 0.241 mV min^{-1} at 1000 mA cm^{-2} voltage loss, while the values for Ir@IrO$_x$/Pt/C and Pt/C + IrO$_2$ are 3.03 and 3.07 mV min^{-1} at 1000 mA cm^{-2}, suggesting enhanced reversal tolerance and better durability for the Ti$_4$O$_7$-supported RTAs. The reversal test principle is illustrated in Fig. 3g for easier understanding. The reversal test was conducted by replacing the H$_2$ with N$_2$ while maintaining a constant current density (200 mA cm^{-2}) to simulate fuel starvation.

EIS at 200 mA cm^{-2} was also conducted to analyze the impedance change before and after the reversal tests. The impedances were fitted by the equivalent circuit model shown in Fig. S12 and S13 (ESI†), and the fitting results are summarized in Table S1 (ESI†). As shown in Fig. S12 (ESI†), the initial impedances are similar for Pt/C + IrO$_2$ and Pt/Ti$_4$O$_7$ + IrO$_2$ anode cells. Qualitatively, the initial ohmic resistances of the samples mentioned above, reflected by the x-left intercepts in the high-frequency region, are almost identical. Furthermore, the diameter of the semicircle represents the charge transfer resistance. In most cases, the charge transfer resistance of the HOR is considerably smaller than that of the ORR because of the faster kinetics.[25,26] This makes isolating the HOR charge transfer resistance challenging unless the anode electron or proton transfer pathways are obstructed. The slight difference in the cathode charge resistance barely affects the polarization performance. After the reversal tests, the impedance of the Pt/C +IrO$_2$ anode cell increases. At the same time, the Pt/Ti$_4$O$_7$ + IrO$_2$ counterpart remains stable, as shown in the hollow point curves in Fig. S12 (ESI†). Specifically, concerning the Pt/C + IrO$_2$ anode cell, the increased resistances lie on the ohmic and the anode charge transfer resistance.

In contrast, the Pt/Ti$_4$O$_7$ + IrO$_2$ anode cell mainly concentrates on the anode charge transfer resistance, indicating the enhanced anode catalyst layer structure protection ability of the Ti$_4$O$_7$ support. When it comes to Ir@IrO$_x$/Pt/C and Ir@IrO$_x$/Pt/Ti$_4$O$_7$ anode cells, there is an analogous situation where the ohmic resistance and anode charge transfer resistance both increase significantly for the Ir@IrO$_x$/Pt/C anode cell, as shown in Fig. S13 (ESI†). By comparison, the ohmic resistance for the Ir@IrO$_x$/Pt/Ti$_4$O$_7$ anode cell barely changes, while the anode charge transfer resistance becomes more prominent. According to the EIS results, the degradation of the Ti$_4$O$_7$-supported anode catalyst layer is not caused by the catalyst layer structure damage, which is validated by SEM images, but due to the obstruction of electron and proton transfer pathways, indicating that the anode catalyst has undergone oxidation. Since the ionomer facilitates the transfer of protons, it is reasonable to infer and consider the resistance to electron transfer.

It is also vital to compare the performance of RTAs multidimensionally and simultaneously, including the Ir loading, first reversal time, and degradation rate. Since the Ir loading represents the cost of RTA fabrication, the reversal time reflects the reversal tolerance ability, and the degradation rate indicates the practical utilization potential. It is meaningless to chase a long reversal time but sacrifice the MEA performance or cease to function after the reversal test because the reversal time is relatively short in the actual operation. It is significant to keep balance among the three parameters. As shown in Fig. 3h and Table S2 (ESI†), the combination of low Ir loading, long reversal time, and slow performance degradation achieved by the Ir@IrO$_x$/Pt/Ti$_4$O$_7$ is comparable to, and in some cases even surpasses, those reported for recent RTAs.[5,14,19,25–38]

2.4 Postmortem characterization and degradation origin

The in-plane and cross-section of anode catalyst layers were scanned using SEM to evaluate the anode catalyst layer destruction, as illustrated in Fig. 4a. For the commercial IrO$_2$ addition
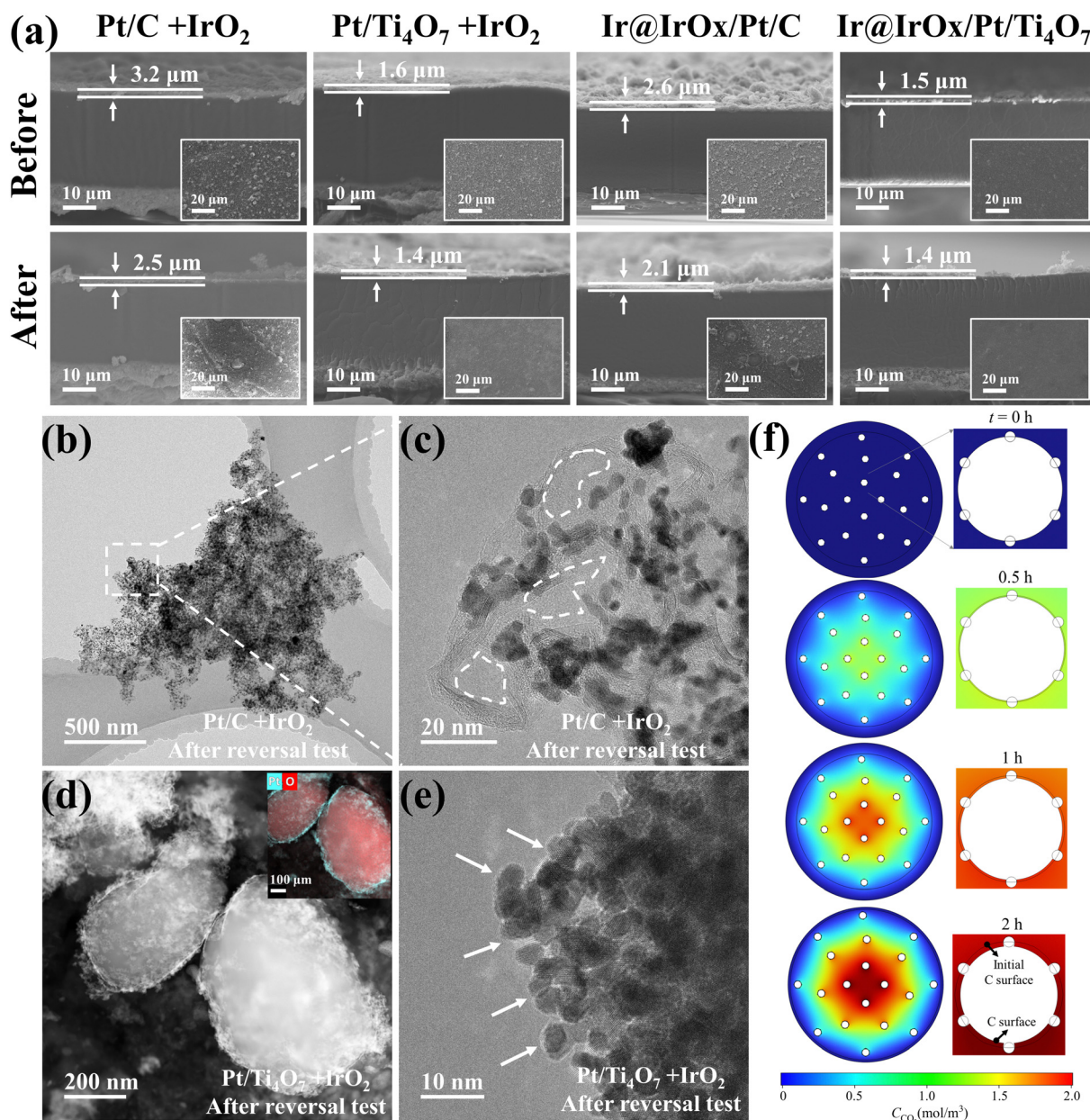
1586 | *Energy Environ. Sci.*, 2024, **17**, 1580–1591

This journal is © The Royal Society of Chemistry 2024

Fig. 4 (a) SEM images of Pt/C +IrO$_2$, Pt/Ti$_4$O$_7$ + IrO$_2$, Ir@IrO$_x$/Pt/C and Ir@IrO$_x$/Pt/Ti$_4$O$_7$ before and after the reversal test. Each inset represents the in-plane anode surface. (b) and (c) TEM images of the Pt/C + IrO$_2$ anode catalyst after the reversal test with different magnifications. (d) and (e) HAADF and TEM images of the Pt/Ti$_4$O$_7$ +IrO$_2$ anode catalyst after the reversal test and the corresponding EDS mapping. (f) CO$_2$ concentration distribution and carbon corrosion as a function of time for the carbon-supported anode catalyst.

samples, micro-size IrO$_2$ is observed in the in-plane images before the reversal tests. The surfaces of the carbon-supported anode catalyst layers become rough and irregular after the reversal tests. At the same time, the darker area is attributed to the adhesive carbon fibers in the GDL, indicating severe carbon corrosion during the reversal test.[6,39] The micro-size holes appear on the carbon-supported anode surface, further suggesting the destruction of catalyst layers. Notable thinner anode catalyst layer thickness is also found when the Pt/C + IrO$_2$ anode decreases from 3.2 μm to 2.5 μm and the Ir@IrO$_x$/Pt/C anode reduces from 2.6 μm to 2.1 μm. By contrast, the

Ti$_4$O$_7$-supported anode catalyst layer displayed a smooth anode catalyst layer surface even though a much longer reversal time was experienced. Meanwhile, a significantly enhanced anode protection ability is found according to the consistent thickness of anode catalyst layers before and after the reversal tests (all approximately 1.5 μm). The SEM characterization further proves the better anode catalyst layer structure retention ability of the Ti$_4$O$_7$-supported catalyst, suggesting the boosted durability when using the Ti$_4$O$_7$ support. After the reversal tests, the TEM images of Pt/C +IrO$_2$ and Pt/Ti$_4$O$_7$ +IrO$_2$ are also shown in Fig. 4b–e and Fig. S14 (ESI†). The characterization focuses on

This journal is © The Royal Society of Chemistry 2024

Energy Environ. Sci., 2024, **17**, 1580–1591 | **1587**

Pt/C +IrO$_2$ and Pt/Ti$_4$O$_7$ +IrO$_2$ anodes since the Ir@IrO$_x$/Pt/C and Ir@IrO$_x$/Pt/Ti$_4$O$_7$ anodes follow a similar degradation phenomenon, but the Ir nanoparticles complicate the morphological observations. As shown in Fig. 4b, the structure of the carbon support becomes spiculate, and the Pt nanoparticles agglomerated with each other in certain areas of the Pt/C +IrO$_2$ anode catalyst after the reversal test. Besides, irregular holes in the higher magnification TEM images appear inside the carbon support structure, as marked with dotted lines in Fig. 4c, suggesting severe carbon corrosion. Moreover, the lattice fringes of carbon intensively appear. In contrast, the amorphous carbon barely shows up, indicating the instability of amorphous carbon under high potential during the reversal test and preferential corrosion of amorphous carbon. In terms of the Pt/Ti$_4$O$_7$ + IrO$_2$ anode, as shown in Fig. 4d, the Ti$_4$O$_7$ support maintains the original structure with a 200 to 300 nm diameter. Meanwhile, the Pt nanoparticles still deposit uniformly on the Ti$_4$O$_7$ surface, as proven by the EDS mapping (Fig. 4d and Fig. S15, ESI†). In addition, the encapsulation of a thin layer of TiO$_x$ covering the Pt particles is observed in the higher magnification TEM image due to the strong metal–support interaction (SMSI),[40] which is indicated by white arrows in Fig. 4e. A multi-physics model was employed utilizing an aggregation model (Fig. S16, ESI†) to gain a more comprehensive understanding of carbon corrosion phenomena. As depicted in Fig. 4f, the CO$_2$ concentration exhibits an increasing trend over time. For instance, the average CO$_2$ concentration within the ionomer domain rises from 0 mol m^{-3} at 0 hours to 1.1 mol m^{-3} at 2 hours. Concurrently, the carbon particle undergoes gradual corrosion as time progresses.

XPS was performed containing Pt 4f, Ti 2p, and O 1s core-level photoemission spectra before and after the reversal tests to compare and investigate the degradation origin of the Ti$_4$O$_7$-supported anode catalyst layer. As shown in Fig. 5, the relative concentrations of different valence states of Pt, Ti and O were calculated based on the spectral weights of the peaks after deconvolution. For Pt 4f, the peak position and deconvolution are presented before, and the content of Pt(0) significantly decreases from more than 60% to 50% after the reversal tests for both Pt/Ti$_4$O$_7$ + IrO$_2$ and Ir@IrO$_x$/Pt/Ti$_4$O$_7$ anodes. By contrast, the content of Pt(ii) rises from approximately 20% to more than 30%. At the same time, Pt(iv) remains stable, suggesting that Pt(0) turns into Pt(ii) and the Pt is oxidized during the reversal test. Furthermore, the peaks of Ti(iii) 2p$_{3/2}$ and Ti(iv) 2p$_{3/2}$ lie at 457.1 eV and 458.5 eV, with a 5.7 eV splitting value variation.[15,41] According to the Ti 2p spectral analysis, the contents of Ti remain steady throughout the reversal test as the Ti(iii) and Ti(iv) contents fluctuate within 1%, which can be considered an experimental system error. The stable Ti(iii) and Ti(iv) contents indicate that the Ti$_4$O$_7$ is hardly oxidized under high potential during the reversal test, consistent with previous research.[14,42] Moreover, the O 1s spectra are also examined to distinguish the peaks of lattice oxygen (530.0 eV), adsorbed oxygen species in the oxygen vacancies (531.4 eV), surface hydroxyl (532.4 eV), and surface water (533.8 eV).[15,43] The surface water peak emerges sharply after the reversal test, attributed to the water generated and
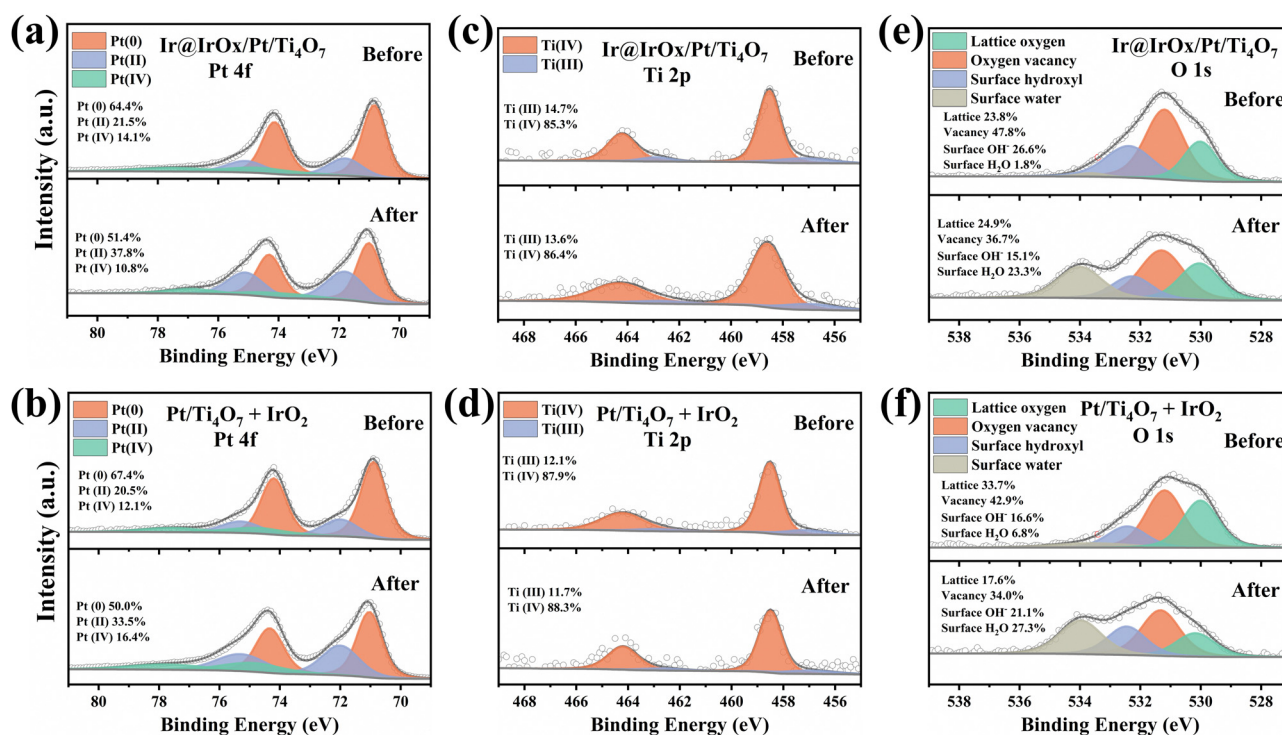

Fig. 5 XPS (a) and (b) Pt 4f, (c) and (d) Ti 2p and (e) and (f) O 1s spectra of Ti$_4$O$_7$-supported catalysts (Ir@IrO$_x$/Pt/Ti$_4$O$_7$ and Pt/Ti$_4$O$_7$ + IrO$_2$) before and after the reversal test.

1588 | *Energy Environ. Sci.*, 2024, **17**, 1580–1591

This journal is © The Royal Society of Chemistry 2024

adsorbed during the test. The oxygen adsorbed on the oxygen vacancy is still dominant even after the reversal tests, suggesting the prominent existence of Ti_4O_7. As previously reported,[40,44,45] the Ti(III) can move to the Pt surface due to the SMSI and form a thin TiO_x layer, which is permeable to proton and hydrogen and will not affect the HOR and Pt hydrogen under potential deposition (H-UPD) formation. According to Fig. S17 (ESI†), the CV tests reveal no significant difference in H-UPD before and after the reversal tests, suggesting normal hydrogen absorption and desorption. Based on these results, the decrease in performance observed after the reversal test is attributed to Pt oxidation. This oxidation occurs due to the formation of a thin layer of TiO_x on the surface of the Pt, which impedes the electron transfer.

3. Conclusions

In this contribution, we synthesized a high specific surface area Ti_4O_7 anode by a facile hydrogen-free method and utilized it as the anode catalyst support. The Ti_4O_7-supported anode catalyst layer parameters were optimized, displaying comparable performance with carbon-supported counterparts. Meanwhile, the screening of Ti_4O_7-supported anode catalyst layers showed enhanced reversal tolerance than a carbon-supported catalyst, whether in traditional IrO_2 addition or novel $Ir@IrO_x/Pt/Ti_4O_7$ core–shell Ir deposition. Specifically, the $Ir@IrO_x/Pt/Ti_4O_7$ RTA presented a 367 min first reversal time and 0.044 mV min^{-1} at 1000 mA cm^{-2} voltage degradation rate, approximately ten times higher and two orders of magnitude lower than those of the $Ir@IrO_x/Pt/C$ RTA under a low Ir loading (0.05 mg$_{Ir}$ cm^{-2}), respectively. Even when applying the traditional IrO_2 addition method, the $Pt/Ti_4O_7 + IrO_2$ RTA still showed a four times longer reversal time and two orders of magnitude lower degradation rate than the $Pt/C + IrO_2$ RTA, maintaining almost identical initial polarization performance. The origin of Ti_4O_7-supported catalyst degradation was also investigated and attributed to the Pt oxidation caused by the formation of TiO_x thin layers at Pt surfaces, which was verified by postmortem EIS, XPS, SEM, and TEM characterizations. This study reveals a novel practical perspective for RTA design by replacing carbon supports. It paves the way for future research of carbon-free anodes for proton exchange membrane fuel cells.

4. Experimental

4.1 Synthesis of the Ti_4O_7 support

Ti_4O_7 was prepared by a facile hydrogen-free method developed elsewhere.[46] Typically, titanyl sulfate ($TiOSO_4$) was applied as the Ti precursor and then hydrolyzed as TiO_2 in water. Subsequently, PEG400 was added under continuous stirring so that TiO_2 was coated with a uniform PEG400 layer. The mass ratio of PEG400 to TiO_2 was kept at 1.5. After that, the water was removed at 80 °C, and the temperature increased to 150 °C for 5 hours. The as-prepared brown powder was ground using an agate mortar and transferred to a sealing quartz crucible.

Then, the sample was heated to 967 °C under pure argon at 10 °C min^{-1}. After the sample was cooled to room temperature, the powder was ground again, then the fine powder was collected.

4.2 Synthesis of Pt/Ti_4O_7 and $IrO_x@Ir/Pt/Ti_4O_7$

Pt/Ti_4O_7 was synthesized by a simple ethanol reduction method. Typically, 18 mg Ti_4O_7 was added into a 500 mL flask containing 200 mL ethanol and 200 mL DI water. After ultra-sonication for 1 hour, $H_2PtCl_6 \cdot xH_2O$ (Sigma-Aldrich, 37.5% Pt content) aqueous solution with 12 mg Pt was added into the above dispersion, which was then stirred for 3 hours at room temperature to obtain a homogeneous solution. Subsequently, the solution was heated to 95 °C for 12 hours. When it cooled down to room temperature, the black powder was collected by vacuum filtration, followed by sufficient hot DI water washing. Lastly, Pt/Ti_4O_7 was obtained by drying at 60 °C overnight.

$IrO_x@Ir/Pt/Ti_4O_7$ was synthesized using the as-prepared Pt/Ti_4O_7. Initially, Pt/Ti_4O_7 was synthesized to support the Ir sol. The weight ratio of Ir to Pt was controlled at 1:2. The Ir sol was obtained using a hydrothermal method with aqueous $IrCl_3 \cdot 3H_2O$ solution (Macklin, 53% Ir content) containing 6 mg Ir and 68 mL of anhydrous ethanol. The solution was mixed and stirred in a 100 mL Teflon-lined stainless steel autoclave and then sealed and maintained at 150 °C for 4 hours. After cooling to room temperature, the prepared Pt/Ti_4O_7 was added to the Ir sol, and the Ir was adsorbed onto the Pt/Ti_4O_7 surface. The mixture was heated to 60 °C with continuous stirring to dry the solvent. It is important to note that nitrogen gas was purged into the mixture during the drying process to prevent the self-ignition of the nano-scale catalysts. The collected powders were annealed at 120 °C for 3 hours to strengthen the metal–support interactions. Finally, the powder was rinsed with deionized water and dried to obtain $IrO_x@Ir/Pt/Ti_4O_7$. Similar treatment proceeded with commercial Pt/C to obtain the $IrO_x@Ir/Pt/C$. For comparison, the $IrO_x@Ir/Ti_4O_7$ was prepared by adding Ti_4O_7 into Ir sol and following the same subsequent processes.

4.3 Characterizations

The surface area of the catalyst was determined by BET analysis using nitrogen isotherms (Micromeritics ASAP 2460). X-ray diffraction (XRD) was performed on a 3 kW Rigaku SmartLab diffractometer with a Cu Kα radiation source at 40 kV and 30 mA at a scan rate of 8° min^{-1}. The electronic conductivity was measured using an automatic powder resistivity tester (Suzhou Jingge Electronic Co. Ltd) with a pressure between 1 MPa and 30 MPa. X-ray photoelectron spectroscopy (XPS) was conducted using a Thermo Fisher ESCALAB Xi+ using mono-chromated Al Kα radiation. Scanning electron microscopy (SEM) images were acquired using a ZEISS Sigma 300 with an accelerating voltage of 5 kV. A Talos F200X G2 was used to obtain the transmission electron microscopy (TEM) images. The TEM images were acquired at 200 kV with the samples deposited on a holey carbon film-covered copper grid. High-resolution transmission electron microscopy (HR-TEM) was conducted using a Titan Themis G2 double spherical

aberration-corrected transmission electron microscope with a 300 kV accelerating voltage.

4.4 Electrode preparation and performance testing

All half-cell tests were conducted in a conventional three-electrode cell with an electrochemical workstation (Shanghai CH Instruments Inc.) on Pine Instruments under room temperature. For the HOR test, the catalyst ink was prepared using isopropyl alcohol, water, and Nafion D520 ionomer. The mass ratio of the ionomer to dry catalyst ink was kept at 30% for the carbon-supported catalyst and IrO_2, and 4% for the Ti_4O_7-supported catalyst. Linear sweep voltammetry (LSV) was performed from 0 to 0.3 V vs. RHE at a scan rate of 5 mV s^{-1} and a rotational rate of 1600 rpm in H_2-saturated 0.1 M $HClO_4$. A glassy carbon electrode (GCE) with a diameter of 5 mm was employed as the working electrode, while a Pt mesh and a reversible hydrogen electrode (RHE) were selected as the counter electrode and reference electrode, respectively. The metal loading was controlled at 20 μg cm^{-2}. A similar protocol was followed for the OER test. The electrolyte and the reference electrode were switched to 0.5 M H_2SO_4 and Ag/AgCl. Besides, the LSV scanning range was adjusted to 1.2 to 1.7 V vs. RHE. The Ir or Pt loading was controlled at 10 μg cm^{-2}.

Regarding the full-cell test, the anode catalyst ink was prepared by ultrasonicating the mixture of the catalyst, D520 Nafion ionomer, and 1:1 water/isopropanol solvent for 1.5 hours. The mass content of ionomer was kept at 30 wt% for Pt/C, Pt/C + IrO_2 and $IrO_x@Ir/Pt/C$, while the same parameter for Pt/Ti_4O_7, Pt/Ti_4O_7 + IrO_2 and $IrO_x@Ir/Pt/Ti_4O_7$ was 4 wt%. The cathode catalyst ink was treated similarly using the 47.1 wt% Pt/C (TEC10EA50E, Tanaka) catalyst. Then, the ink was sprayed onto both sides of the proton exchange membrane (Nafion 211, 25 μm, Chemours) with an effective area of 4 cm^2. The Pt loading was controlled at 0.1 mg$_{Pt}$ cm^{-2} and 0.4 mg$_{Pt}$ cm^{-2} for the anode and cathode, respectively. The catalyst-coated membrane (CCM) and gas diffusion layers (MB30, AvCarb) were assembled to form the MEA. Two pieces of Teflon with 150 μm thickness were used as sealing gaskets to prevent gas leakage. The single-cell tests were all conducted on a Hephas HTS-125 fuel cell test station at 80 °C with 100% relative humidity (RH). Back pressures of hydrogen and air were 100 kPa. For the cell reversal test, 0.4 L min^{-1} nitrogen and 0.2 L min^{-1} air were supplied at the anode and cathode, during which the outlets of both the anode and cathode were exposed to ambient pressure. A constant current density of 0.2 A cm^{-2} was applied, and the cell voltage was recorded using an electrochemical workstation (Solartron EnergyLab XM). Then, the cell would shut down when the voltage reached −2.0 V.[30,47] The polarization performance, cyclic voltammetry (CV), and electrochemical impedance spectroscopy (EIS) tests were conducted before and after the cell reversal tests. The EIS was performed at 200 mA cm^{-2} under fully humidified H_2/air, and the frequency was scanned from 100 kHz to 0.1 Hz. The CV was conducted in fully humidified N_2/H_2 with fixed flows and ambient pressure, scanning from 0.1 to 1.0 V at a scan rate of 50 mV s^{-1}. To evaluate the polarization performance, two flow rate conditions were tested (fixed flows of 0.5/1 L min^{-1} and stoichiometry of 1.5/2.5) for comparison. The fixed flow test was carried out, ensuring ample provision of gases to address the mass transfer problem. Meanwhile, the stoichiometry flow test provided a practical condition to assess the actual performance.

Conflicts of interest

There are no conflicts to declare.

Acknowledgements

References

1 I. Staffell, D. Scamman, A. Velazquez Abad, P. Balcombe, P. E. Dodds, P. Ekins, N. Shah and K. R. Ward, Energy Environ. Sci., 2019, 12, 463–491.

2 K. Jiao, J. Xuan, Q. Du, Z. Bao, B. Xie, B. Wang, Y. Zhao, L. Fan, H. Wang, Z. Hou, S. Huo, N. P. Brandon, Y. Yin and M. D. Guiver, Nature, 2021, 595, 361–369.

3 Z. Li, Y. Wang, Y. Mu, B. Wu, Y. Jiang, L. Zeng and T. Zhao, Renewable Sustainable Energy Rev., 2023, 176, 113182.

4 P. Ren, P. Pei, Y. Li, Z. Wu, D. Chen and S. Huang, Prog. Energy Combust. Sci., 2020, 80, 100859.

5 C. Cai, Y. Rao, J. Zhou, L. Zhang, W. Chen, Z. Wan, J. Tan and M. Pan, J. Power Sources, 2020, 473, 228542.

6 Y. Wang, C. Zhou, X. Xie, C. Yang, Q. Feng, J. Zou, X.-Z. Yuan, J. Fan, L. Zeng, H. Li and H. Wang, Int. J. Hydrogen Energy, 2020, 45, 996–1007.

7 Z. Li, H. Huang, Y. Wang, Y. Mu, Y. Jiang, Q. Zhang, T. Zhao and L. Zeng, Chem. Eng. J., 2023, 144189.

8 S. Ye, in PEM Fuel Cell Electrocatalysts and Catalyst Layers: Fundamentals and Applications, ed. J. Zhang, Springer, London, 2008, pp. 835–860.

9 H. J. Liu, M. Q. Luo, L. X. Yang, C. L. Zeng and C. Fu, Ceram. Int., 2022, 48, 25538–25546.

10 F. C. Walsh and R. G. A. Wills, Electrochim. Acta, 2010, 55, 6342–6351.

11 J. E. Graves, D. Pletcher, R. L. Clarke and F. C. Walsh, J. Appl. Electrochem., 1991, 21, 848–857.

12 X. Sun, Z. Wang, W. Yan and C. Zhou, Catalysts, 2022, 12, 480.

1590 | Energy Environ. Sci., 2024, 17, 1580–1591

This journal is © The Royal Society of Chemistry 2024

13 J.-E. Won, D.-H. Kwak, S.-B. Han, H.-S. Park, J.-Y. Park, K.-B. Ma, D.-H. Kim and K.-W. Park, *J. Catal.*, 2018, **358**, 287–294.

14 T. Ioroi and K. Yasuda, *J. Power Sources*, 2020, **450**, 227656.

15 S.-H. You, S.-M. Jung, K.-S. Kim, J. Lee, J. Park, H. Y. Jang, S. Shin, H. Lee, S. Back, J. Lee and Y.-T. Kim, *ACS Energy Lett.*, 2023, 2201–2213.

16 S.-Y. Huang, P. Ganesan, S. Park and B. N. Popov, *J. Am. Chem. Soc.*, 2009, **131**, 13898–13899.

17 F. T. Angerasa, C.-Y. Chang, E. A. Moges, W.-H. Huang, K. Lakshmanan, Y. Nikodimos, J.-F. Lee, N. G. Habtu, M.-C. Tsai, W.-N. Su and B. J. Hwang, *Mater. Today Energy*, 2023, **34**, 101312.

18 B. M. Stühmeier, A. M. Damjanović, K. Rodewald and H. A. Gasteiger, *J. Power Sources*, 2023, **558**, 232572.

19 Y. Li, W. Song, G. Jiang, Y. Yang, H. Yu, Z. Shao, F. Duan and Y. Yang, *Front. Energy*, 2022, **16**, 852–861.

20 Z. Wang, X. Jin, F. Chen, X. Kuang, J. Min, H. Duan, J. Li and J. Chen, *J. Colloid Interface Sci.*, 2023, **650**, 901–912.

21 C. Wang, Z. X. Liu, Z. Q. Mao, J. M. Xu and K. Y. Ge, *Chem. Eng. J.*, 2005, **112**, 87–91.

22 Y. Wang, J. Jin, S. Yang, G. Li and J. Qiao, *Electrochim. Acta*, 2015, **177**, 181–189.

23 Z. Liu, L. M. Gan, L. Hong, W. Chen and J. Y. Lee, *J. Power Sources*, 2005, **139**, 73–78.

24 C. E. Moore, F. Afsahi, A. P. Young and E. L. Gyenge, *J. Phys. Chem. C*, 2019, **123**, 23361–23373.

25 Y. Wang, J. Liao, Z. Li, B. Wu, J. Lou, L. Zeng and T. Zhao, *Int. J. Hydrogen Energy*, 2022, **47**, 13101–13111.

26 J. Liao, S. Zaman, Y. Wang, M. Yang, L. Yang, M. Chen and H. Wang, *ACS Appl. Mater. Interfaces*, 2023, **15**, 4092–4100.

27 C. Cai, Z. Wan, Y. Rao, W. Chen, J. Zhou, J. Tan and M. Pan, *J. Power Sources*, 2020, **455**, 227952.

28 B. K. Hong, P. Mandal, J.-G. Oh and S. Litster, *J. Power Sources*, 2016, **328**, 280–288.

29 X. Zhou, H. Ji, B. Li and C. Zhang, *ACS Omega*, 2020, **5**, 10099–10105.

30 P. Mandal, B. K. Hong, J.-G. Oh and S. Litster, *J. Power Sources*, 2018, **397**, 397–404.

31 Y. Li, L. Zhao, X. Du, W. Gao, C. Zhang, H. Chen, X. He, C. Wang and Z. Mao, *Chem. Eng. J.*, 2023, **461**, 141823.

32 Y. Wang, Y. Jiang, J. Liao, Z. Li, T. Zhao and L. Zeng, *ACS Appl. Mater. Interfaces*, 2022, **14**, 56867–56876.

33 J. Wang, X. Zhou, B. Li, D. Yang, H. Lv, Q. Xiao, P. Ming, X. Wei and C. Zhang, *Int. J. Hydrogen Energy*, 2020, **45**, 8930–8940.

34 C.-W. Roh, H.-E. Kim, J. Choi, J. Lim and H. Lee, *J. Power Sources*, 2019, **443**, 227270.

35 W. Chen, C. Cai, S. Li, J. Tan and M. Pan, *Int. J. Hydrogen Energy*, 2021, **46**, 8749–8757.

36 E. You, M. Min, S.-A. Jin, T. Kim and C. Pak, *J. Electrochem. Soc.*, 2018, **165**, F3094–F3099.

37 K. H. Lim, W. H. Lee, Y. Jeong and H. Kim, *J. Electrochem. Soc.*, 2017, **164**, F1580–F1586.

38 T. Labi, F. Van Schalkwyk, S. M. Andersen, P. Morgen, S. C. Ray and J. Chamier, *J. Power Sources*, 2021, **490**, 229568.

39 Y. Wang, X. Xie, C. Zhou, Q. Feng, Y. Zhou, X.-Z. Yuan, J. Xu, J. Fan, L. Zeng, H. Li and H. Wang, *J. Power Sources*, 2020, **449**, 227542.

40 B. M. Stühmeier, S. Selve, M. U. M. Patel, T. N. Geppert, H. A. Gasteiger and H. A. El-Sayed, *ACS Appl. Energy Mater.*, 2019, **2**, 5534–5539.

41 M. C. Biesinger, L. W. M. Lau, A. R. Gerson and R. St. C. Smart, *Appl. Surf. Sci.*, 2010, **257**, 887–898.

42 T. Arai, O. Takashi, K. Amemiya and T. Takahashi, *SAE Int. J. Alt. Power.*, 2017, **6**, 145–150.

43 Y. Zhu, L. Zhang, B. Zhao, H. Chen, X. Liu, R. Zhao, X. Wang, J. Liu, Y. Chen and M. Liu, *Adv. Funct. Mater.*, 2019, **29**, 1901783.

44 T. N. Geppert, M. Bosund, M. Putkonen, B. M. Stühmeier, A. T. Pasanen, P. Heikkilä, H. A. Gasteiger and H. A. El-Sayed, *J. Electrochem. Soc.*, 2020, **167**, 084517.

45 B.-J. Hsieh, M.-C. Tsai, C.-J. Pan, W.-N. Su, J. Rick, H.-L. Chou, J.-F. Lee and B.-J. Hwang, *Electrochim. Acta*, 2017, **224**, 452–459.

46 M. Chisaka, W. Nagano, B. Delgertsetseg and T. Takeguchi, *Chem. Commun.*, 2021, **57**, 12772–12775.

47 X. Zhou, Y. Yang, B. Li and C. Zhang, *ACS Appl. Mater. Interfaces*, 2021, **13**, 2455–2461.

This journal is © The Royal Society of Chemistry 2024

Energy Environ. Sci., 2024, **17**, 1580–1591 | 1591